

Reversing ferroelectric polarization in multiferroic DyMn_2O_5 by nonmagnetic Al substitution of Mn

Z. Y. Zhao, M. F. Liu, X. Li, J. X. Wang, Z. B. Yan, K. F. Wang, and J. –M. Liu^{a)}

Laboratory of Solid State Microstructures, Nanjing University, Nanjing 210093, China

[Abstract] The multiferroic RMn_2O_5 family, where R is rare-earth ion or Y, exhibits rich physics of multiferroicity which has not yet well understood, noting that multiferroicity is receiving attentions for promising application potentials. DyMn_2O_5 is a representative member of this family. The ferroelectric polarization in DyMn_2O_5 is claimed to have two anti-parallel components: one (P_{DM}) from the symmetric exchange striction between the Dy^{3+} - Mn^{4+} interactions and the other (P_{MM}) from the symmetric exchange striction between the Mn^{3+} - Mn^{4+} interactions. We investigate the evolutions of the two components upon a partial substitution of Mn^{3+} by nonmagnetic Al^{3+} in order to tailor the Mn-Mn interactions and then to modulate component P_{MM} in $\text{DyMn}_{2-x/2}\text{Al}_{x/2}\text{O}_5$. It is revealed that the ferroelectric polarization can be successfully reversed by the Al-substitution via substantially suppressing the Mn^{3+} - Mn^{4+} interactions and thus the P_{MM} . The Dy^{3+} - Mn^{4+} interactions and the polarization component P_{DM} can sustain against the substitution until a level as high as $x=0.2$. In addition, the independent Dy spin ordering is shifted remarkably down to an extremely low temperature due to the Al^{3+} substitution. The present work not only confirms the existence of the two anti-parallel polarization components but also unveils the possibility of tailoring them independently.

PACS numbers: 75.85.+t, 77.80.B-, 77.22.Ej, 75.25.-j

Keywords: DyMn_2O_5 , multiferroics, Mn-Mn interactions, polarization reversal.

^{a)} To whom all correspondences should be addressed, E-mail: liujm@nju.edu.cn

I. Introduction

In recent years there has been an upsurge in research into multiferroic materials that display coupling between magnetic and ferroelectric orders [1, 2]. In particular, those multiferroics with magnetically induced electric polarization (so-called type-II multiferroics) have been receiving attention [2-4]. Rare-earth manganites RMn_2O_5 (RMO) represent a specific class of such materials featured with large electric polarization and complicated magnetic interactions [5-10], with respect to other well known multiferroics such as RMnO_3 [11-13], LiCu_2O_2 [14], and MnWO_4 [15] etc. Due to the complexities in lattice structure and magnetic interactions, our understanding of the microscopic mechanisms underlying the ferroelectricity and the complicated magnetic transitions of RMn_2O_5 is still in a stage of continuous updating, which needs substantial efforts [16-18].

It is noted that all the members of the RMn_2O_5 family have similar structural ingredients [10, 19]. The Mn ions are partitioned into Mn^{3+} and Mn^{4+} , which are coordinated respectively in square pyramid Mn-O units and octahedral Mn-O units. The octahedra and pyramids are corner-sharing by either the pyramid base or pyramid apex, and the adjacent pyramids are connected with their bases. Along the c -axis, the octahedra sharing edges constitute linear chains. Each Mn^{3+} ion is located in between two Mn^{4+} ions, and the R^{3+} ions are located on the alternative layer between two Mn^{4+} ions. Therefore, RMn_2O_5 can be written as $\text{R}^{3+}\text{Mn}^{3+}\text{Mn}^{4+}_2\text{O}_5$. Obviously, the two structural blocks (pyramid Mn-O units and octahedral Mn-O units) stack alternatively and constitute different stacking sequences along the three orthogonal axes, making a number of degrees of freedom for structural distortions and magnetic interactions [16, 20]. The multifold competing interactions in RMn_2O_5 mainly arise from the multi-valance states of Mn and serious lattice distortions associated with the above mentioned structural ingredients, resulting in a set of complicated magnetic transitions. If the R ion has large magnetic moment, the magnetic transitions can be even more complicated due to the non-negligible R-Mn interactions, noting that the $4f$ -magnetism is quite different from the $3d$ -magnetism [21].

For a detailed illustration, we take DyMn_2O_5 as an example, and the ab -plane projected structural model is shown in Fig.1(a) where the Dy and Mn spin structures are schematically plotted, referred to the lattice and spin structures data from literature [22]. It is seen that the

lattice accommodates the interactions from the $\text{Mn}^{3+}\text{-Mn}^{4+}$, $\text{Mn}^{4+}\text{-Mn}^{4+}$, $\text{Mn}^{3+}\text{-Mn}^{3+}$, $\text{Dy}^{3+}\text{-Mn}^{4+}$, $\text{Dy}^{3+}\text{-Mn}^{3+}$, and $\text{Dy}^{3+}\text{-Dy}^{3+}$ pairs. The paramagnetic phase above temperature $T \sim 43\text{K}$ transits into an incommensurate antiferromagnetic (IC-AFM) phase, followed by a commensurate AFM (C-AFM) phase below $T_{N1} \sim 40\text{K}$, and then by the coexistence of an IC-AFM phase and a C-AFM phase below $T_{N2} \sim 28\text{K}$. This coexistence is again replaced by two coexisting IC-AFM phases below $T_{N3} \sim 20\text{K}$. At $T < T_{Dy} \sim 8\text{K}$, the Dy^{3+} spins order independently [18]. Recently, the noncollinear Mn spin order with helical or cycloidal geometry in DyMn_2O_5 was reported [19]. The ferroelectric transitions associated with the magnetic transition sequence were investigated, and so far reported data are somehow controversial [7, 8]. Both the C-AFM and IC-AFM phases can be ferroelectric although the IC-AFM phase may not. Basically, the electric polarization P most likely aligns along the b -axis, but its T -dependence appears to be complicated and no consistency is reached owing to the lacking of sufficient data [7, 8, 23].

Even though those unclear issues mentioned above are under investigations, a simplified scenario on the ferroelectricity can be outlined, regardless of the details of the magnetic transitions around T_{N2} and T_{N3} . It is not strange that the ferroelectricity in RMn_2O_5 has complicated origins. In fact, earlier first-principles calculations predicted an electric polarization much larger than measured one. The reason is that the polarization has two anti-parallel components which originate respectively from the electronic and ionic contributions [24]. On the other hand, it was suggested that the Mn-Mn and Dy-Mn interactions both make contributions to the ferroelectricity via the symmetry exchange strictions, as schematically shown in Fig.1(c)-(d) [23]. The whole lattice structure can be mapped into a spatial pattern filled with two types of block groups alternatively. One is block A which consists of a $\text{Mn}^{4+}\text{-O}$ octahedron sandwiched with two $\text{Dy}^{3+}\text{-O}$ units, and the other is block B which consists of a $\text{Mn}^{4+}\text{-O}$ octahedron sandwiched with two $\text{Mn}^{3+}\text{-O}$ pyramids. The spins in the block A ($\text{Dy}^{3+}\text{-Mn}^{4+}\text{-Dy}^{3+}$) roughly align in the $\downarrow\downarrow\uparrow$ or $\uparrow\uparrow\downarrow$ pattern along the b -axis although there are small components along the a -axis and c -axis, generating a local electric dipole as indicated by the inner-open arrow P_{DM} in Fig.1(c). The spin alignment in the block B ($\text{Mn}^{3+}\text{-Mn}^{4+}\text{-Mn}^{3+}$) takes roughly the $\downarrow\uparrow\uparrow$ or $\uparrow\downarrow\downarrow$ pattern along the b -axis too, as shown in Fig.1(d), generating a local electric dipole as indicated by the inner-open arrow P_{MM} .

The two types of electric dipoles are roughly anti-parallel to each other. It is noted that the two types of block groups stack alternatively and occupy the whole lattice. The macroscopic ferroelectric polarization P has two anti-parallel components P_{DM} and P_{MM} . Therefore, DyMn_2O_5 is basically a ferrielectric rather than a normal ferroelectric [7, 23].

The above model on the magnetically induced ferroelectricity may be still simplified and details of the correlations between the ferroelectricity and magnetic transitions around T_{N2} and T_{N3} are in fact not yet understood. We don't deal with these details in this work, and our major concern goes to the qualitative scenario with which the origin of P_{DM} and P_{MM} can be understood and the tuning possibility can be explored. Recently, the ferrielectricity of DyMn_2O_5 was discussed in the above model framework with the measured electric polarization $P=P_{DM}+P_{MM}$, and their T -dependences are schematically shown in Fig.2 [23]. Polarization P is negative at $T<T_{NI}$ and becomes positive at low T , giving a sign reversal at certain point $T_{P=0}$. It is because of $P_{MM}>0$ and $P_{DM}<0$ so that their superposition ($P=P_{DM}+P_{MM}$) constitutes the complicated T -dependence and sign reversal at $T_{P=0}$. What motivates us here is how to modulate the electric polarization using some approaches, in particular the possibility of reversing/tailoring the polarization.

In attempt to tailor the electric polarization, however, the complexity is added by the independent Dy spin ordering below T_{Dy} [7, 8, 23]. On one hand, the independent Dy spin ordering destabilizes significantly the $\downarrow\downarrow\uparrow$ and $\uparrow\uparrow\downarrow$ -type $\text{Dy}^{3+}\text{-Mn}^{4+}\text{-Dy}^{3+}$ spin order in block A, thus suppressing partially the polarization component P_{DM} . This partial suppression is the reason for the anomalous slowing-down of the increasing tendency of P with decreasing T below T_{Dy} , as shown in Fig.2 for a guide of eyes, noting that this increasing tendency would be otherwise continuing, as shown by the P' as a function of T . However, due to the weak $\text{Dy}^{3+}\text{-Dy}^{3+}$ interaction, the independent Dy spin ordering is sensitive to the structural and magnetic perturbations and can be easily destabilized. It is suggested that any tailoring approach, if effective in tailoring the two polarization components P_{MM} and P_{DM} , may impose substantial impact on the independent Dy spin ordering as a side-effect.

Looking back at Fig.1, one sees that the $\text{Mn}^{4+}\text{-O}$ octahedron is centered at the units of the two types of blocks. It is imagined that a substitution of Mn^{4+} may disorder the spin alignments in both the block A and block B, thus damaging the P_{MM} and P_{DM} unfavorably for

the ferroelectricity. If any approach to substitute partially Dy^{3+} or Mn^{3+} is taken, one of the two types of blocks would be tailored while the other may sustain without much change, as long as the substitution is limited at a low level. Surely, such a tailoring approach must rely on structural perturbations as small as possible, which is yet tough if not impossible. This is the main motivation for the present work.

We consider the Al^{3+} -substitution of Mn, since Al^{3+} is nonmagnetic and its ionic radius is only slightly smaller than Mn^{3+} (Mn^{4+}), so that the change of lattice environment remains small. We shall demonstrate a reversal of electric polarization in DyMn_2O_3 by gradually removing the $\downarrow\uparrow\uparrow$ or $\uparrow\downarrow\downarrow$ alignment in the block B, as tentatively shown in Fig.1(e), where component P_{MM} disappears gradually but component P_{DM} survives. Furthermore, this substitution also lowers the stability of the independent Dy spin order below T_{Dy} , making the component P_{DM} to follow the T -dependence of P'_{DM} shown in Fig.2. The present approach obviously allows a reversing of the ferroelectric polarization while the substitution strategy is so simple.

In this work, we prepare a series of polycrystalline $\text{DyMn}_{2-x/2}\text{Al}_{x/2}\text{O}_5$ samples. It will be shown that the Al^{3+} ions most likely replace Mn^{3+} ions rather than Mn^{4+} ions, as revealed by various structural and chemical characterizations. The measured data on the electric and magnetic properties confirm a successful reversal of the ferroelectric polarization by partially substituting Mn^{3+} with Al^{3+} . Furthermore, several additional multiferroic behaviors are observed, suggesting rich physics in terms of ferroelectric response to the tailoring of magnetic orders.

II. Experimental details

A. Samples preparation & structural characterization

A series of polycrystalline $\text{DyMn}_{2-x/2}\text{Al}_{x/2}\text{O}_5$ samples were prepared by standard solid state sintering. Stoichiometric amount of Dy_2O_3 (99.99%), Mn_2O_3 (99%), and Al_2O_3 (99.99%) was thoroughly mixed (ground), compressed into pellets, and sintered at 1200°C for 24 h in a flowing oxygen atmosphere with several cycles of intermediate grindings. For every sintering cycle, the samples were cooled down to room temperature at a rate of 100°C per hour from the sintering temperature. The as-prepared samples were cut into various shapes for

subsequent microstructural and property characterizations. For structural characterization, the crystallinity was checked using X-ray diffraction (XRD) with Cu $K\alpha$ radiation at room temperature and the high-resolution data were used for structural Rietveld refining by the GSAS program. The atomic ratios and chemical valence states of Mn species were probed using the X-ray photoelectron spectroscopy (XPS, PHI500 Versa Probe, UIVAC-PHI Inc.) with the monochromatic Al $K\alpha$ radiation. Particular attention was paid to the relative variations of the $\text{Mn}^{3+}/\text{Mn}^{4+}$ ions so that the Al-substitution of Mn^{3+} site can be checked.

B. Measurements of magnetic and electric properties

The specific heat (C_p), magnetization (M) and dc magnetic susceptibility (χ), dielectric constant (ϵ) and electric polarization (P) of the samples were characterized. The M and χ were measured using the Quantum Design Superconducting Quantum Interference Device (SQUID) in the zero-field cooled (ZFC) mode and field-cooling (FC) mode, respectively. Both the cooling field and measuring field are 1.0kOe. The C_p was measured using the Quantum Design Physical Properties Measurement System (PPMS) in the standard procedure.

Here the measurement of pyroelectric current $I_{pyro}(T)$ was critical since the ferroelectric polarization $P(T)$ was evaluated from the $I_{pyro}(T)$ data. Each sample was polished into a thin disk of 0.2mm in thickness and 10mm in diameter, and then sandwich-coated with Au layers as top and bottom electrodes. The measurement was performed using the Keithley 6514A and 6517 electrometers connected to the PPMS and the related details were described in Ref. [23]. The pre-poling electric field E_{pole} was 10kV/cm and the samples were cooled under the electric poling down to $T_{end}=2\text{K}$. It is noted that the as-prepared polycrystalline samples are highly insulating and the recorded background current noise amplitude was less than 0.2pA. The polarization $P(T)$ was obtained by integrating the collected $I_{pyro}(T)$ data, from $T_0 \gg T_{NI}$ down to T_{end} .

The validity of this procedure was confirmed repeatedly in earlier works and here it is confirmed again. Fig.3 shows the measured $I_{pyro}(T)$ data at three warming rates (2, 4, 6K/min) for sample $x=0.0$. It comes to our attention that the three curves, if normalized by the corresponding warming rate, almost perfectly overlap with each other, showing no difference between them within the measuring uncertainties and less than 0.3K peak-to-peak shift along

the T -axis. These peaks are sharp and well fixed while thermally stimulated currents other than the pyroelectric current are usually broad. These features indicate that the measured data do come from the pyroelectric current without identifiable contribution from other sources. In addition, the measured I_{pyro} - T curve can be switched upon a reversed poling field.

In addition, the $\alpha(T)$ data at various frequencies were collected with an *ac*-bias of ~ 50 mV. Besides the $\alpha(T)$ data and $P(T)$ data, we also measured the response of P to magnetic field H in two modes. One is the isothermal mode with which the variation in P in response to the scanning of H was detected and the other is the iso-field mode with which the P - T data under a fixed H were collected. By such measurements, one can evaluate the ME coupling by defining $\Delta P(H) = P(H) - P(H=0)$ as the magnetoelectric (ME) parameter.

III. Results and discussion

A. Structural distortion and chemical valence states

We first check the crystallinity and associated lattice distortion. The XRD θ - 2θ spectra for several samples are plotted in Fig.4(a). While all these reflections can be indexed by the standard database of orthorhombic DyMn_2O_5 lattice, and gradual peak shifts towards the high-angle side are observed. It is noted that the Al-substitution of Mn up to $x=0.20$ does not change the lattice symmetry. The inset in Fig.4(b) shows the local peaks at $2\theta \sim 29^\circ$ for $x=0.00$, 0.10, and 0.16, and the local peak profiles are almost the same although the profile shifts gradually rightward with increasing x . We perform the Rietveld refining of the data and one example is given for sample $x=0.04$, as shown in Fig.4(b). The refining reliability is as high as $R_{wp}=4.48\%$. The evaluated lattice unit volume V as a function of x , plotted in Fig.3(c), decreases gradually, due to the slightly smaller ionic size of Al^{3+} than Mn ion, and the fitted errors are reasonably small. What should be mentioned here is that the $V(x)$ seems to be slightly nonlinear rather than linear as predicted by the Vegard's law, suggesting that the possible cation charge valence variation upon the Al-substitution can't be excluded although this variation may be ascribed to the variation of magnetic interactions via the spin-lattice coupling. Therefore, careful checking of the charge valence of Mn and Al should be made.

We consult to the XPS determination of Mn ions in valence state upon the Al-substitution. The data on all these samples show no trace of intensity from the Mn^{5+} or Mn^{2+} within the

apparatus resolution. Since the binding energies for the $\text{Mn}^{3+}2p_{1/2}/\text{Mn}^{4+}2p_{1/2}$ and $\text{Mn}^{3+}2p_{3/2}/\text{Mn}^{4+}2p_{3/2}$ are very close respectively [25], a highly reliable fitting of the XPS peaks associated with Mn is required. Fig.5(a) show this fitting for sample $x=0.0$, in which the $2p_{1/2}$ and $2p_{3/2}$ peaks are assumed to be the superimposition of the contributions from the Mn^{3+} and Mn^{4+} . It is seen that the sum of the shadow areas below the peaks $\text{Mn}^{3+}2p_{1/2}$ and $\text{Mn}^{3+}2p_{3/2}$ is roughly equal to that below the peaks $\text{Mn}^{4+}2p_{1/2}$ and $\text{Mn}^{4+}2p_{3/2}$, indicating that the $\text{Mn}^{3+}:\text{Mn}^{4+}$ ratio is close to the nominal value. The same fitting procedure is applied to the other samples and the fitted $\text{Mn}^{3+}:\text{Mn}^{4+}$ ratios are consistent with the nominal ones with an uncertainty of $\pm 5\%$.

Alternatively, we present in Fig.5(b) the amplified Mn $2p_{3/2}$ peaks for several samples to see the overall tendency of the peak shift. Indeed no trace signals from Mn^{5+} or Mn^{2+} are seen. The gradual shifting of the peak towards the high-energy side with increasing x is concededly identified, indicating more Mn^{4+} ions than Mn^{3+} ions in the samples with higher x . This behavior provides direct evidence on the claim that the Al^{3+} ions substitute the Mn^{3+} ions rather than Mn^{4+} ions. Although one can't exclude the possibility for tiny occupation of the Mn^{4+} sites by Al^{3+} , the present XPS data demonstrate that the Al^{3+} -occupation of Mn^{3+} is dominant, favored from the point of view of charge balance.

B. Anomalies of multiferroic properties at the magnetic phase transitions

Before proceeding to the Al-substitution effects, we first look at the anomalies of several parameters at the magnetic phase transitions. The normalized specific heat C_P/T , magnetization M (under ZFC and FC modes both), dielectric permeability ε , pyroelectric current I_{pyro} (I_{tot}), and electric polarization P , are plotted in Fig.6. For a reference, the ferroelectric phases in various T -ranges are marked on the top row, including the recently confirmed ferroelectric X-phase [8, 23]. Parameters C_P/T , ε , I_{pyro} , and P , all show clear anomalies at the magnetic phase transition points T_{N1} , T_{N2} , T_{N3} , and T_{Dy} . However, the $M(T)$ curves are trivial except the broad peak at T_{Dy} . This behavior is well known and the reason is that the paramagnetic fluctuations from the Dy spins above T_{Dy} are dominant, submerging the anomalies from the Mn spin ordering. The anomalies of ε , I_{pyro} , and P at these transition points reflect the ME coupling. In particular, the anomalies of the $I_{pyro}(T)$ curve at T_{N1} , T_{N2} ,

T_{N3} , and T_{Dy} , as shown in Fig.6(d), are one-to-one corresponding to those in the $C_p/T(T)$ curves but more remarkable than the latters.

For sample $x=0.0$, earlier experiments established the correlations between these peaks in the $I_{pyro}(T)$ curve, the ferroelectric transitions associated with P_{MM} and P_{DM} , and the magnetic phase transitions [23]. A brief description is given here as an additional illustration to Fig.2. First, the sharp negative current peak right below T_{N1} indicates the generation of P_{MM} (<0) due to the development of roughly collinear Mn^{3+} - Mn^{4+} - Mn^{3+} spin order and the P_{MM} tends to be saturated at $T \sim T_{N2}$ and below. Second, the broad positive current bump around T_{N2} seems to sign the generation of P_{DM} (>0) due to the development of the Dy^{3+} - Mn^{4+} - Dy^{3+} spin order and the P_{DM} increases continuously with decreasing T . Third, a Dy-Mn spin coupling occurs which can be understood as the Dy spin ordering induced by the Mn spin orders. This induced Dy spin ordering may initiate above T_{N2} but develop well below T_{N3} . However, details of this coupling remain unclear. Fourth, the sharp positive peak around T_{Dy} signs the consequence of the independent Dy spin ordering, which can damage the collinear Dy^{3+} - Mn^{4+} - Dy^{3+} spin order and thus the P_{DM} , while the P_{MM} is less affected. What should be answered is the question why the $I_{pyro}(T)$ peak right below T_{N1} is negative, i.e. $P_{MM} < 0$. The reason is that $P_{DM} > P_{MM}$ at $T_{end} \sim 2K$ and therefore the cooling under electric poling down to T_{end} enables the P_{DM} to align along the poling field but P_{MM} is antiparallel to the field, i.e. $P_{MM} < 0$ [23]. In Fig.6(e), the P_{MM} and P_{DM} as a function of T respectively are plotted and $P = P_{MM} + P_{DM}$. In the following, one will see that these correlations are the basis on which the effects of Al-substitution are understood.

We first investigate the effect of Al-substitution on the independent Dy spin ordering at T_{Dy} . The $M-T$ data at several x values are plotted in Fig.7. It is seen that the T_{Dy} is indeed suppressed with increasing x . For $x=0.20$, T_{Dy} falls down to $\sim 2K$ and below. At the first glance this phenomenon seems unusual and our evidence supports that the Al ions substitute the Mn ions rather than the Dy ions. Nevertheless, due to the high sensitivity of the independent Dy spin ordering to weak perturbations of lattice and spin interactions [21], the Al-substitution seems to generate such perturbations sufficient for disordering this order. This implies that the Al-substitution most likely removes the influence of the independent Dy spin ordering on the ferroelectricity (mainly component P_{DM}), enabling the physics simpler. The tendency of

$P_{DM} \rightarrow P'_{DM}$ and $P \rightarrow P'$, as predicted in Fig.2, will be confirmed below.

C. Ferroelectric polarizations

Now we focus on the electric polarization in response to the Al-substitution. The P - T data for a series of samples are plotted in Fig.8(a)-(g). We also insert the $I_{pyro}(T)$ data for sample $x=0.0$ in each plot for a comparison so that the change of the $I_{pyro}(T)$ curve with increasing x can be identified easily.

Several interesting characters of the $I_{pyro}(T)$ curve and $P(T)$ curve with increasing x are worthy of addressing. First, as expected, the negative current peak right below T_{NI} is remarkably suppressed and downshifted with increasing x , indicating the suppression of the ferroelectric transitions associated with the P_{MM} . At $x \sim 0.08$ and above, the negative current peak becomes nearly disappeared. Correspondingly, component P_{MM} becomes disappear. It is suggested that the Al-substitution does succeed in breaking the Mn^{3+} - Mn^{4+} - Mn^{3+} collinear spin order. Second, the positive current peak around T_{Dy} in sample $x=0.0$, as indicated by the arrow in Fig.8(a), becomes very weak in sample $x=0.02$ and disappeared in sample $x=0.04$ and other samples with higher x . Referring to the magnetic data shown in Fig.7, it is suggested that the peak disappearance at $x \geq 0.04$ is attributed to the Al-substitution induced downshifting of the independent Dy spin ordering. This feature is consistent with the predicted P' as a function of T in Fig.2. Third, the broad current bump around T_{N3} in sample $x=0.0$ is evolved into a sharp peak locating in-between T_{N2} and T_{N3} for low x level ($x < 0.08$). It is found that, upon increasing x from 0.0 to 0.08, this positive peak increases in height and shifts rightward, in compensation with the height decreasing and leftward shifting of the negative peak around T_{NI} . Eventually, the two peaks meet and annihilate with each other. The last ‘moment’ of the two peak annihilation is shown in Fig.8(d) at $x=0.08$. One easily understands that the two peaks correspond respectively to the polarization generation at the higher- T side (negative current peak) and polarization disappearance at the lower- T side (positive current peak). The simultaneous evolution of the two peaks illustrates how the P_{MM} is suppressed upon the Al-substitution, as shown in Fig.8(a)~(d).

In accompanying with the serious suppression of the P_{MM} , the evolution of the P_{DM} is different, although a quantitative evaluation is impossible since we only have the $P(T)$ data.

Without doubt, the Al-substitution certainly damages the P_{DM} too because the spin structure is anyhow diluted by the Al^{3+} ions. This effect can be seen in Fig.8, and the measured P in the low- T range does not increase much while the negative P_{MM} is seriously suppressed by the Al-substitution. Since $P=P_{DM}+P_{MM}$, it is clear that the $P_{DM}(T)$ decreases with increasing x . As $x \geq 0.08$, only the P_{DM} is left while the P_{MM} is completely suppressed. However, the P_{DM} is much more robust than the P_{MM} against the Al-substitution and the $P_{DM} > 100 \mu\text{C}/\text{m}^2$ at 2K is retained even $x=0.20$. This implies that the Al-substitution does not change much the collinear $\text{Dy}^{3+}\text{-Mn}^{4+}\text{-Dy}^{3+}$ spin order. To show this, the as-evaluated maximal P_{DM} and P_{MM} values are plotted as a function of x in Fig.9. Unfortunately, further increasing of x generates impurity phase and the stability of this spin order over the whole x -range may be concerned by other approaches.

D. Polarization reversal

It is interested to note that the significant impact of the Al-substitution on P_{MM} as described above leads to a negative-positive reversal of polarization P , which is illustrated by plotting the $P(x)$ curves at several T , as shown in Fig.8(h). The $P(T=2\text{K})$ data are always positive due to $P_{DM} > P_{MM}$, but both the $P(T=15\text{K})$ and $P(T \sim T_{N3})$ reverse their signs from negative to positive at certain x ($x \sim 0.04$ and 0.065). The successful reversal can be more clearly seen by the phase-diagram in Fig.10. The whole phase-diagram is divided into three regions. Given $P_{MM} < 0$ and $P_{DM} > 0$, one has $P=(P_{MM}+P_{DM}) < 0$ while $|P_{MM}| \gg |P_{DM}|$ in region I. In region II, $|P_{MM}| > |P_{DM}|$ is replaced by $|P_{MM}| < |P_{DM}|$ so we have $P=(P_{MM}+P_{DM}) > 0$. A crossing through the boundary between regions I and II is accompanied with a reversal of polarization P . One has $P_{MM} \sim 0$ so $P > 0$ in region III, while $P_{DM} \sim 0$ and $P_{MM} \sim 0$ are expected as $x > 0.20$. The coarse solid double-head arrow indicates a reversal of polarization P while the dashed double-head arrow shows the generation/disappearance of component P_{MM} associated with the Mn-Mn interactions.

One may address that such a polarization reversal in multiferroics with magnetically induced ferroelectricity has rarely been observed so far and this is the first experimental evidence for the polarization reversal by chemical substitution. While the complexity of the multiferroic physics in DyMn_2O_5 is well known [7, 8], here we present a simple example for

this physics, which allows a direct manipulation of the ferroelectric polarization in RMn_2O_5 .

E. Magnetoelectric response

Keeping in mind the motivations and consequences of the Al-substitution in DyMn_2O_5 , additional evidence with the proposed physics therein can be obtained from the magnetoelectric response. As noted earlier, the Dy^{3+} - Dy^{3+} spin interaction is quite weak and thus a remarkable response of the Dy^{3+} spin order to magnetic field is expected. Differently, the $\text{Mn}^{3+}/\text{Mn}^{4+}$ spins are much more robust [8, 23]. This argument can be checked here since P_{MM} is nearly zero in region III (Fig.10), by measuring the magnetoelectric response. We present in Fig.11 the $P(T)$ data obtained at several H in the iso-field mode, for three samples $x=0.0$, 0.12, and 0.16.

One can easily understand the observed results in Fig.11. For sample $x=0.0$, the consequence of applying a magnetic field should be the rapid suppression of P from positive to negative in the low- T range while no big variation of P in the high- T range [23]. The data in the left column do confirm this consequence, and the P value at $T=2\text{K}$ falls from $\sim 120\mu\text{C}/\text{m}^2$ under $H=0$ to $-95\mu\text{C}/\text{m}^2$ under $H=5\text{T}$, noting that the anomalous slowing-down effect of P below T_{Dy} becomes disappeared as $H>1.0\text{T}$. For sample $x=0.12$, noting no more P_{MM} available, the measured P initiates roughly at $T_{N3}<T<T_{N2}$ and then gradually increases with decreasing T , indicating the ferroelectric phase transitions associated with P_{DM} , as shown in the middle column of Fig.11. No anomaly of the $P(T)$ dependence below T_{Dy} is detected, obviously due to the absence of the independent Dy spin ordering. The electric polarization is remarkably suppressed upon implication of magnetic field, by a change of $\sim 50\%$ at $H=5.0\text{T}$. It is noted that the ferroelectric transition point does not change much. Similar behaviors are identified for sample $x=0.16$ and the magnetoelectric response is even more remarkable, as seen in the right column of Fig.11. For both the latter two cases, the measured P remains positive under a field as high as $H=9.0\text{T}$, very different from the case observed for sample $x=0.0$.

The complete disappearance of the electric polarization is expected when the substitution is higher than $x=0.20$, which is not available unfortunately for us at the current synthesis conditions. On the other hand, extremely high magnetic field is expected to suppress

completely the polarization. Nevertheless, the so far available data are sufficient to confirm the proposed model (Fig.1 and Fig.2) and the phase diagram Fig.10, while the non-magnetic Al-substitution of Mn demonstrates its capability to reverse the electric polarization.

F. Discussion

It is highly agreed that DyMn_2O_5 and other RMn_2O_5 family members are complicated in terms of magnetic structures and ferroelectricity origins [16, 18]. However, the proposed model and the simple substitution strategy in this work enable our understanding of the physics of multiferroicity in a quite simplified framework. This framework seems to catch up the core of the physics, although the details of those relatively weak anomalies of magnetic and dielectric responses around T_{N2} and T_{N3} are not considered.

This simple strategy is essentially associated with the magnetic structure highlighted in Fig.1, noting that similar magnetic structure in RMn_2O_5 members with $\text{R}=\text{Gd}$, Tb , Ho , and Er , was reported recently [26-30]. In this sense, the present model would be of generality to some extent. Indeed, this model can be used to explain quite a number of multiferroic behaviors in these materials, but many of them can't yet be reasonably predicted and interpreted. The possible reasons for these failures include the following aspects. First, the R ionic size variation is critical for the lattice distortion and thus the delicate balance of the multifold interactions. Second, the $4f$ - $3d$ coupling between R and Mn ions can be very different for different members. The Gd-Mn, Dy-Mn, and Ho-Mn couplings are strong while the Tb-Mn and Er-Mn couplings are relatively weak [26, 31]. For the latter cases, the polarization component P from the R-Mn coupling could be quite small and thus the underlying physics becomes different. In this sense, the lattice would accommodate a normal ferroelectric behavior rather than the ferrielectricity. Third, clear noncollinear spin components in these materials, as shown in Fig.1 for DyMn_2O_5 , may contribute to the electric polarization via the spin-orbit coupling mechanism [20], which is not taken into account in the present work. This contribution, if available, would make the ferroelectric phase transitions and response of P to T and H different from the collinear three-spin block mechanisms addressed here. For example, the low-field response of P (Fig.11) may be more favorably contributed by this noncollinear mechanism. These issues deserve for further investigations, which, however, on

the contrary suggests the substantial significance of the present experiments based on such a simple scenario.

IV. Conclusion

In conclusion, we have investigated in details the effects of Al^{3+} substitution of Mn ions on the magnetic and ferroelectric behaviors in multiferroic DyMn_2O_5 , based on the proposed model for ferrielectricity generation. It is revealed that structurally the Al^{3+} substitution favors the Mn^{3+} sites rather than Mn^{4+} ions, and makes the lattice contracting slightly. This tiny structural distortion seems to suppress remarkably the independent Dy spin ordering which enters below $T_{\text{Dy}} \sim 8\text{K}$ in DyMn_2O_5 . In consequence, the ferrielectric lattice decomposes gradually into a normal ferroelectric lattice by disappearance of the polarization component P_{DM} , due to the gradual disordering of the $\downarrow\downarrow\uparrow$ or $\uparrow\uparrow\downarrow$ collinear $\text{Mn}^{3+}(\text{Al}^{3+})\text{-Mn}^{4+}\text{-Mn}^{3+}(\text{Al}^{3+})$ spin blocks, while the $\downarrow\downarrow\uparrow$ or $\uparrow\uparrow\downarrow$ collinear $\text{Dy}^{3+}\text{-Mn}^{4+}\text{-Dy}^{3+}$ spin blocks are maintained in the lattice. It is demonstrated that the simple strategy of the Al-substitution of Mn can be an effective approach to tune the electric polarization and reverse it from negative value to positive one. The present work provides a comprehensive understanding of the multiferroicity in DyMn_2O_5 and may shed light on efficient approaches to be taken for improving the multiferroic performances of the whole RMn_2O_5 systems.

Acknowledgement:

This work was supported by the National 973 Projects of China (Grants No. 2011CB922101), the Natural Science Foundation of China (Grants Nos. 11234005, 11374147, and 51332006), and the Priority Academic Program Development of Jiangsu Higher Education Institutions, China.

References:

1. S. W. Cheong and M. Mostovoy, *Multiferroics: a magnetic twist for ferroelectricity*, Nature Mater. 6, 13 (2007).
2. G. Q. Zhang, S. Dong, Z. B. Yan, Y. Y. Guo, Q. F. Zhang, S. Yunoki, E. Dagotto, and J. –M. Liu, *Multiferroic properties of $\text{CaMn}_7\text{O}_{12}$* , Phys. Rev. B 84, 174413 (2011).
3. T. Kimura, T. Goto, H. Shintani, K. Ishizaka, T. Arima, and Y. Tokura, *Magnetic control of ferroelectric polarization*, Nature (London) 426, 55 (2003).
4. D. Khomskii, *Trends: classifying multiferroics: mechanisms and effects*, Physics 2, 20 (2009).
5. N. Hur, S. Park, P. A. Sharma, J. S. Ahn, S. Guha, and S. W. Cheong, *Electric polarization reversal and memory in a multiferroic material induced by magnetic fields*, Nature (London) 429, 392 (2004).
6. M. Fukunaga, Y. Sakamoto, H. Kimura, Y. Noda, N. Abe, K. Taniguchi, T. Arima, S. Wakimoto, M. Takeda, K. Kakurai, and K. Kohn, *Magnetic-field-induced polarization flop in multiferroic TmMn_2O_5* , Phys. Rev. Lett. 103, 077204 (2009).
7. N. Hur, S. Park, P. A. Sharma, S. Guha, and S. W. Cheong, *Colossal magnetodielectric effects in DyMn_2O_5* , Phys. Rev. Lett. 93, 107207 (2004).
8. D. Higashiyama, S. Miyasaka, N. Kida, T. Arima, and Y. Tokura, *Control of the ferroelectric properties of DyMn_2O_5 by magnetic fields*, Phys. Rev. B 70, 174405 (2004).
9. K. F. Wang, J. –M. Liu, and Z. F. Ren, *Multiferroicity: the coupling between magnetic and ferroelectric orders*, Adv. Phys. 58, 321 (2009).
10. Y. Noda, H. Kimura, M. Fukunaga, S. Kobayashi, I. Kagomiya, and K. Kohn, *Magnetic and ferroelectric properties of multiferroic RMn_2O_5* , J. Phys. Condens. Matt. 20, 434206 (2008).
11. T. Goto, T. Kimura, G. Lawes, A. P. Ramirez, and Y. Tokura, *Ferroelectricity and giant magnetocapacitance in perovskite rare-earth manganites*, Phys. Rev. Lett. 92, 257201 (2004).
12. O. Prokhnenko, R. Feyerherm, E. Dudzik, S. Landsgesell, N. Aliouane, L. C. Chapon, and D. N. Argyriou, *Enhanced ferroelectric polarization by induced Dy spin order in*

- Multiferroic DyMnO₃*, Phys. Rev. Lett. 98, 057206 (2007).
13. B. Lorenz, Y. Q. Wang, and C. W. Chu, *Ferroelectricity in perovskite HoMnO₃ and YMnO₃*, Phys. Rev. B 76, 104405 (2007).
 14. S. Park, Y. J. Choi, C. L. Zhang, and S. W. Cheong, *Ferroelectricity in an S=1/2 chain cuprate*, Phys. Rev. Lett. 98, 057601 (2007).
 15. K. Taniguchi, N. Abe, H. Sagayama, S. Ohtani, T. Takenobu, Y. Iwasa, and T. Arima, *Magnetic-field dependence of the ferroelectric polarization and spin-lattice coupling in multiferroic MnWO₄*, Phys. Rev. B 77, 064408 (2008).
 16. A. B. Sushkov, M. Mostovoy, R. V. Aguilar, S. W. Cheong, and H. D. Drew, *Electromagnons in multiferroic RMn₂O₅ compounds and their microscopic origin*, J. Phys. Condens. Matter 20, 434210 (2008).
 17. J. H. Kim, S. H. Lee, S. I. Park, M. Kenzenlmann, A. B. Harris, J. Schefer, J. H. Chung, C. F. Majkrzak, M. Takeda, S. Wakimoto, S. Y. Park, S. W. Cheong, M. Matsuda, H. Kimura, Y. Noda, and K. Kakurai, *Spiral spin structures and origin of the magnetoelectric coupling in YMn₂O₅*, Phys. Rev. B 78, 245115 (2008).
 18. W. Ratcliff II, V. Kiryukhin, M. Kenzelmann, S. -H. Lee, R. Erwin, J. Schefer, N. Hur, S. Park, and S. W. Cheong, *Magnetic phase diagram of the colossal magnetoelectric DyMn₂O₅*, Phys. Rev. B 72, 060407(R) (2005).
 19. P. G. Radaelli and L. C. Chapon, *A neutron diffraction study of RMn₂O₅ multiferroics*, J. Phys. Condens. Matter 20, 434213 (2008).
 20. G. R. Blake, L. C. Chapon, R. G. Radaelli, S. Park, N. Hur, and S. W. Cheong, *Spin structure and magnetic frustration in multiferroic RMn₂O₅ (R=Tb, Ho, Dy)*, Phys. Rev. B 71, 214402 (2005).
 21. R. A. Ewing, A. T. Boothroyd, D. F. McMorrow, D. Mannix, H. C. Walker, and B. M. R. Wanklyn, *X-ray resonant diffraction study of multiferroic DyMn₂O₅*, Phys. Rev. B 77, 104415 (2008).
 22. G. E. Johnstone, R. A. Ewing, R. D. Johnson, C. Mazzoli, H. C. Walker, and A. T. Boothroyd, *Magnetic structure of DyMn₂O₅ determined by resonant x-ray scattering*, Phys. Rev. B 85, 224403 (2012).
 23. Z. Y. Zhao, M. F. Li, X. Li, L. Lin, Z. B. Yan, S. Dong, and J. -M. Liu, *Experimental*

- observation of ferrielectricity in multiferroic DyMn₂O₅*, Sci. Rep. 4, 3984. (2014).
24. G. Giovannetti and J. van den Brink, *Electronic correlations decimate the ferroelectric polarization of multiferroic HoMn₂O₅*, Phys. Rev. Lett. 100, 227603 (2008).
 25. T. Taniguchi, S. Mizusaki, N. Okada, Y. Nagata, S. H. Lai, M. D. Lan, N. Hiraoka, M. Itou, Y. Sakurai, T. C. Ozawa, Y. Noro, and H. Samata, *Crystallographic and magnetic properties of the mixed-valence oxides CaRu_{1-x}Mn_xO₃*, Phys. Rev. B 77, 014406 (2008).
 26. N. Lee, C. Vecchini, Y. J. Choi, L. C. Chapon, A. Bombardi, P. G. Radaelli, and S. W. Cheong, *Giant tunability of ferroelectric polarization in GdMn₂O₅*, Phys. Rev. Lett. 110, 137203 (2013).
 27. L. C. Chapon, G. R. Blake, M. J. Gutmann, S. Park, N. Hur, P. G. Radaelli, and S. W. Cheong, *Structural anomalies and multiferroic behavior in magnetically frustrated TbMn₂O₅*, Phys. Rev. Lett. 93, 177402 (2004).
 28. C. Vecchini, L. C. Chapon, P. J. Brown, T. Chatterji, S. Park, S. W. Cheong, and P. G. Radaelli, *Commensurate magnetic structures of RMn₂O₅ (R=Y, Ho, Bi) determined by single-crystal neutron diffraction*, Phys. Rev. B 77, 134434 (2008).
 29. U. Staub, Y. Bodenthin, M. García-Fernández, R. A. de Souza, M. Garganourakis, E. I. Golovenchits, V. A. Sanina, and S. G. Lushnikov, *Magnetic order of multiferroic ErMn₂O₅ studied by resonant soft x-ray Bragg diffraction*, Phys. Rev. B 81, 144401 (2010).
 30. C. J. Wang, G. C. Guo, and L. X. He, *Ferroelectricity driven by the noncentrosymmetric magnetic ordering in multiferroic TbMn₂O₅: a first-principles study*, Phys. Rev. Lett. 99, 177202 (2007).
 31. R. D. Johnson, C. Mazzoli, S. R. Bland, C-H. Du, and P. D. Hatton, *Magnetically induced electric polarization reversal in multiferroic TbMn₂O₅: Terbium spin reorientation studied by resonant x-ray diffraction*, Phys. Rev. B 83, 054438 (2011).

Figure Captions

Fig.1. A schematic drawing of the spin structure at low T and possible mechanisms for electric polarization generation. (a) The spin structure projected on the ab plane, and these structural units are not on the same lattice plane and they alternatively shift roughly $1/2$ or $-1/2$ atomic layer distance along the c -axis. (b) The structural unit symbols used in (a). (c) The two sub-types of block A, and the local electric dipoles P_{DM} due to the symmetric exchange striction associated with the $\downarrow\downarrow\uparrow$ and $\uparrow\uparrow\downarrow$ $\text{Dy}^{3+}\text{-Mn}^{4+}\text{-Dy}^{3+}$ spin alignments, respectively. (d) The two sub-types of block B, and the local electric dipoles P_{MM} due to the symmetric exchange striction associated with the $\downarrow\uparrow\uparrow$ and $\uparrow\downarrow\downarrow$ $\text{Mn}^{3+}\text{-Mn}^{4+}\text{-Mn}^{3+}$ spin alignments, respectively. (e) The two sub-types of block C with the Al-substituted $\text{Mn}^{3+}\text{-Mn}^{4+}\text{-Al}^{3+}$ chains which have no electric dipole. The lattice of DyMn_2O_5 thus accommodates a ferrielectricity.

Fig.2. The predicted T -dependence of electric polarization P as a feature of ferrielectricity, where polarization P consists of two anti-parallel components P_{DM} and P_{MM} . It is suggested that these polarizations should take the dependences P' , P'_{DM} and P_{DM} if no independent Dy spin ordering would occur below T_{Dy} .

Fig.3. Measured pyroelectric current $I_{pyro}(T)$ for DyMn_2O_5 with warming rate of 2K/min (a), 4K/min (a), and 6K/min (a).

Fig.4. (a) Measured XRD θ - 2θ spectra for a series of $\text{DyMn}_{2-x}\text{Al}_x\text{O}_5$ samples with labeled x values. (b) The Rietveld refined data for sample $x=0.04$ and the insert shows the local reflections of three samples $x=0.00$, 0.10, and 0.16. (c) The fitted unit volume V as a function of x with a fitting curve for guide of eyes.

Fig.5. (a) Measured XPS spectrum for sample $x=0.0$ as an example, where the Mn^{3+} and Mn^{4+} core energy levels are labeled and the measured peaks are decomposed as the superimposition of the contributions from the Mn^{3+} and Mn^{4+} excitations, respectively. (b) The local peaks around 642 eV corresponding to the Mn ($2p_{3/2}$) core level. The peak shifting toward the high

energy with increasing x is shown, indicating the increasing $\text{Mn}^{4+}/\text{Mn}^{3+}$ ratio.

Fig.6. Measured specific heat C_P/T (a), magnetization M (b), dielectric constant ε (c), pyroelectric current I_{pyro} (d), and evaluated electric polarization P (e), as a function of T respectively, for sample $x=0.0$. The decomposed P_{DM} and P_{MM} are shown in (e) [??].

Fig.7. Measured magnetization M for samples $x=0, 0.04, 0.08$, and 0.20 , as a function of T respectively.

Fig.8. Measured pyroelectric current $I_{pyro}(T)$ and evaluated polarization $P(T)$ for a series of samples in (a)~(g), where the $I_{pyro}(T)$ data for sample $x=0.0$ are inserted for reference. The P data at several temperatures as a function of x are plotted in (h).

Fig.9. Evaluated P_{MM} and P_{DM} as a function of x respectively at $T=2\text{K}$.

Fig.10. The measured phase diagram on the (x, T) space. The crossing between region I and region II is indicated by the solid double head arrow, suggesting the reversing of electric polarization P . In region III, no more polarization component P_{MM} is available.

Fig.11. Measured $P(T)$ data under various magnetic field H for sample $x=0.0$ (left column), $x=0.12$ (middle column), and $x=0.16$ (right column).

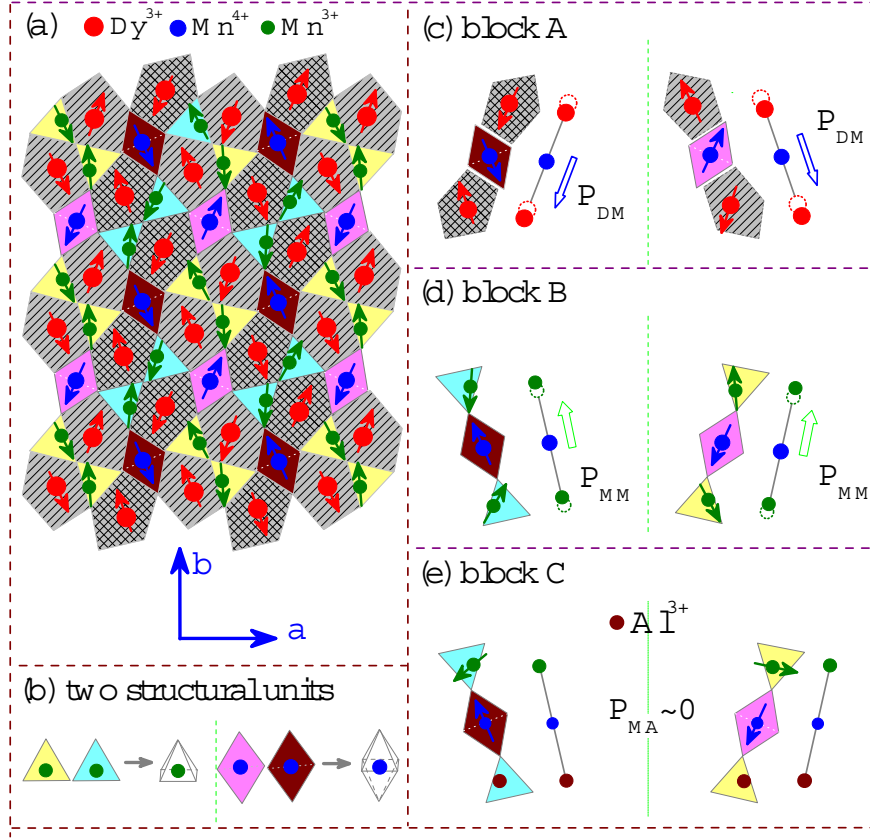


Fig.1. A schematic drawing of the spin structure at low T and possible mechanisms for electric polarization generation. (a) The spin structure projected on the ab plane, and these structural units are not on the same lattice plane and they alternatively shift roughly $1/2$ or $-1/2$ atomic layer distance along the c -axis. (b) The structural unit symbols used in (a). (c) The two sub-types of block A, and the local electric dipoles P_{DM} due to the symmetric exchange striction associated with the $\downarrow\downarrow\uparrow$ and $\uparrow\uparrow\downarrow$ Dy^{3+} - Mn^{4+} - Dy^{3+} spin alignments, respectively. (d) The two sub-types of block B, and the local electric dipoles P_{MM} due to the symmetric exchange striction associated with the $\downarrow\uparrow\uparrow$ and $\uparrow\downarrow\downarrow$ Mn^{3+} - Mn^{4+} - Mn^{3+} spin alignments, respectively. (e) The two sub-types of block C with the Al-substituted Mn^{3+} - Mn^{4+} - Al^{3+} chains which have no electric dipole. The lattice of DyMn_2O_5 thus accommodates a ferrielectricity.

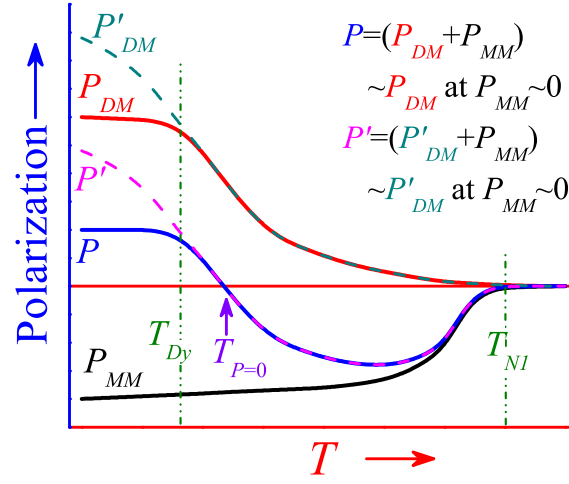


Fig.2. The predicted T -dependence of electric polarization P as a feature of ferrielectricity, where polarization P consists of two anti-parallel components P_{DM} and P_{MM} . It is suggested that these polarizations should take the dependences P' , P'_{DM} and P_{DM} if no independent Dy spin ordering would occur below T_{Dy} .

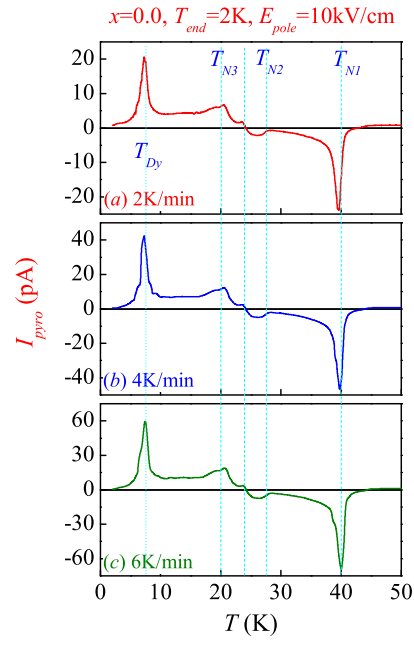


Fig.3. Measured pyroelectric current $I_{pyro}(T)$ for $DyMn_2O_5$ with warming rate of 2K/min (a), 4K/min (a), and 6K/min (a).

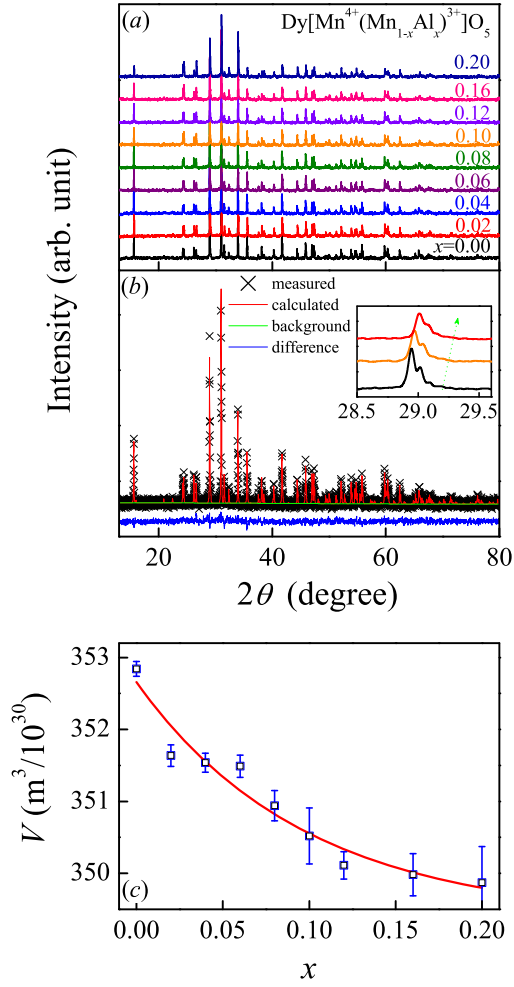


Fig.4. (a) Measured XRD θ - 2θ spectra for a series of $\text{DyMn}_{2-x}\text{Al}_x\text{O}_5$ samples with labeled x values. (b) The Rietveld refined data for sample $x=0.04$ and the insert shows the local reflections of three samples $x=0.00$, 0.10, and 0.16. (c) The fitted unit volume V as a function of x with a fitting curve for guide of eyes.

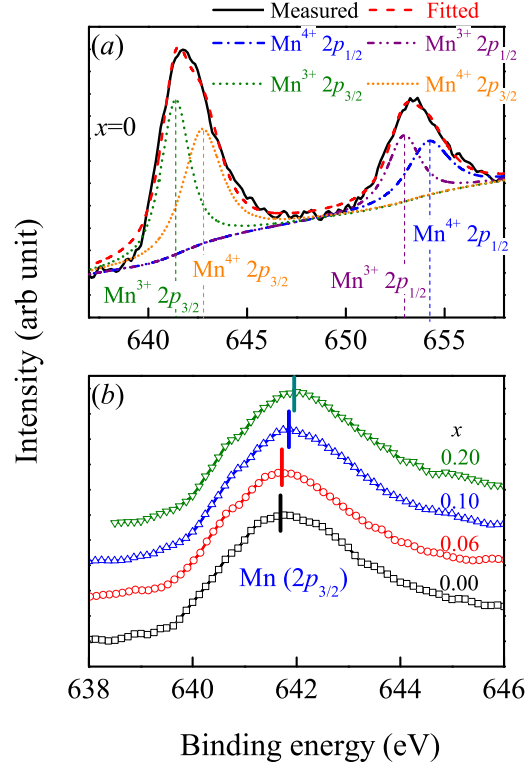


Fig.5. (a) Measured XPS spectrum for sample $x=0.0$ as an example, where the Mn^{3+} and Mn^{4+} core energy levels are labeled and the measured peaks are decomposed as the superimposition of the contributions from the Mn^{3+} and Mn^{4+} excitations, respectively. (b) The local peaks around 642 eV corresponding to the $\text{Mn} (2p_{3/2})$ core level. The peak shifting toward the high energy with increasing x is shown, indicating the increasing $\text{Mn}^{4+}/\text{Mn}^{3+}$ ratio.

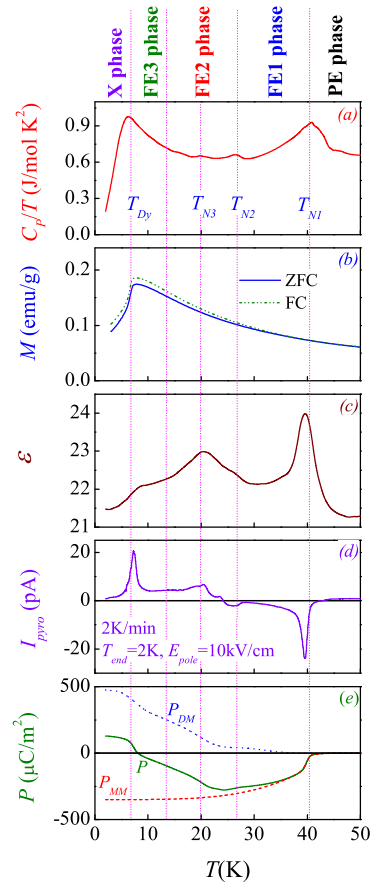


Fig.6. Measured specific heat C_p/T (a), magnetization M (b), dielectric constant ε (c), pyroelectric current I_{pyro} (d), and evaluated electric polarization P (e), as a function of T respectively, for sample $x=0.0$. The decomposed P_{DM} and P_{MM} are shown in (e) [??].

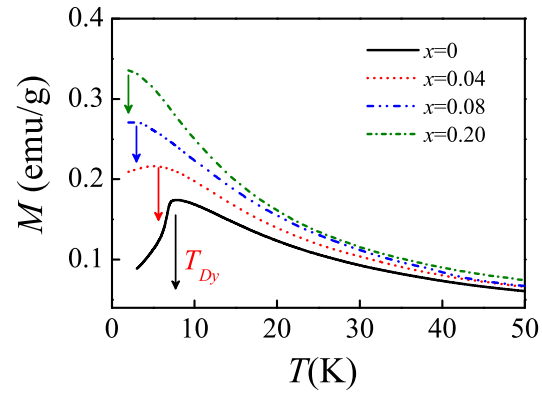


Fig.7. Measured magnetization M for samples $x=0$, 0.04, 0.08, and 0.20, as a function of T respectively.

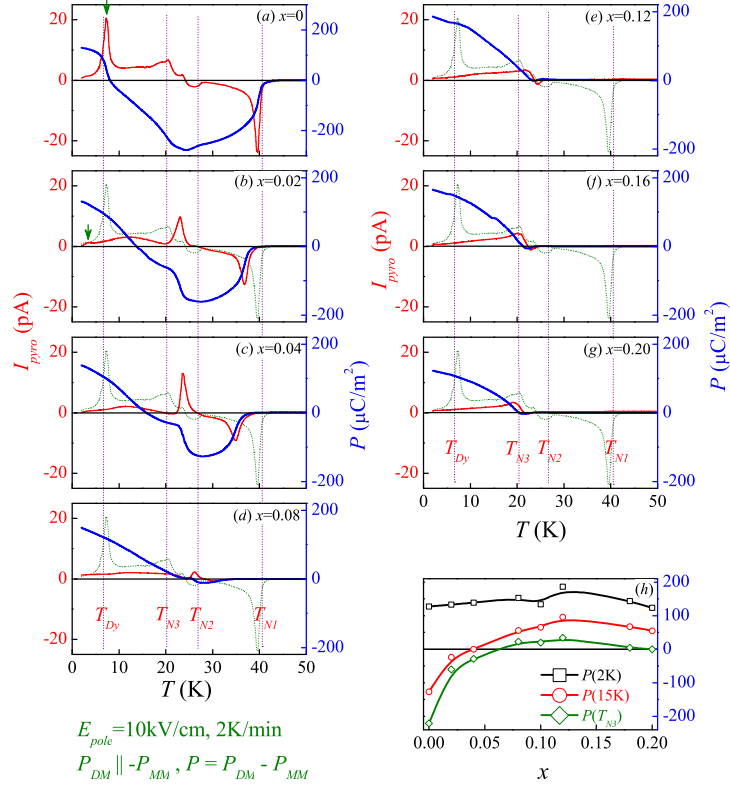


Fig.8. Measured pyroelectric current $I_{pyro}(T)$ and evaluated polarization $P(T)$ for a series of samples in (a)~(g), where the $I_{pyro}(T)$ data for sample $x=0.0$ are inserted for reference. The P data at several temperatures as a function of x are plotted in (h).

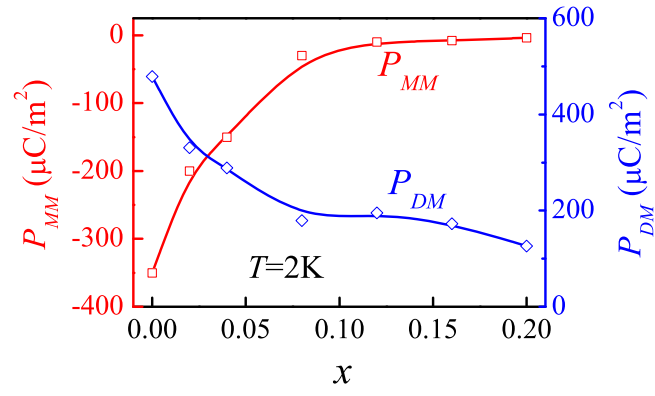


Fig.9. Evaluated P_{MM} and P_{DM} as a function of x respectively at $T=2\text{K}$.

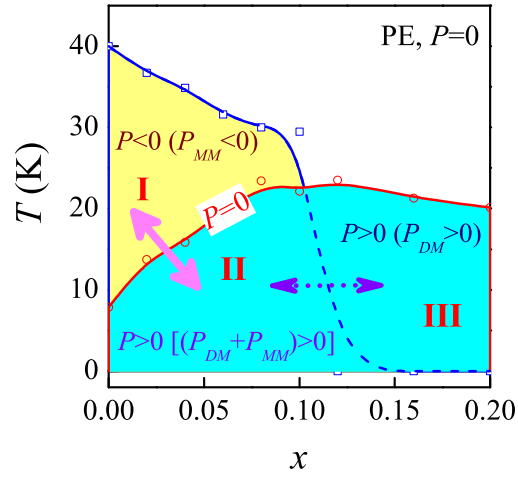


Fig.10. The measured phase diagram on the (x, T) space. The crossing between region I and region II is indicated by the solid double head arrow, suggesting the reversing of electric polarization P . In region III, no more polarization component P_{MM} is available.

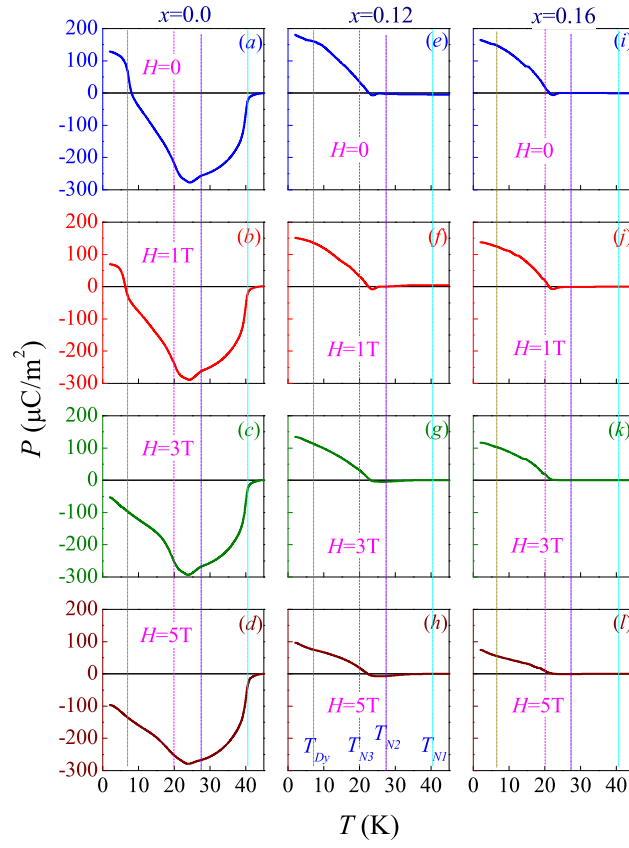


Fig.11. Measured $P(T)$ data under various magnetic field H for sample $x=0.0$ (left column), $x=0.12$ (middle column), and $x=0.16$ (right column).